Journal of Materials Chemistry C

ROYAL SOCIETY OF CHEMISTRY

PAPER

View Article Online
View Journal | View Issue

Cite this: J. Mater. Chem. C, 2024, 12, 9255

Isomeric modulation of thermally activated delayed fluorescence in dibenzo[*a*,*c*]phenazine-based (deep) red emitters†

Sonny Brebels, [abc] Tom Cardeynaels, [abcd] Louis Jackers, [abc] Suman Kuila, [e] Huguette Penxten, [abc] Rebecca J. Salthouse, [f] Andrew Danos, *[e] Andrew P. Monkman, [e] Benoît Champagne [d] and Wouter Maes *[abc]

A series of four emissive regio-isomers are synthesized based on the dibenzo[*a*,*c*]phenazine-11,12-dicarbonitrile (**DBPzCN**) acceptor scaffold and a triphenylamine (TPA) donor. Density functional theory is utilized to compare the relative differences in molecular conformation, excited state distributions, and orbital interactions. Steady-state and time-resolved emission spectroscopy reveal strongly contrasting emissive properties and triplet harvesting of the four materials. In zeonex host emission maxima range widely, with differences of over 100 nm. Additionally, isomers **3-TPA-DBPzCN** and **4-TPA-DBPzCN** show photoluminescence quantum yields (PLQYs) of 46 and 62%, while **1-TPA-DBPzCN** and **2-TPA-DBPzCN** instead show values <1 and 24%, respectively. Relevant to thermally activated delayed fluorescence (TADF), very small singlet–triplet energy gaps are observed for isomers **2-TPA-DBPzCN** and **4-TPA-DBPzCN**, with corresponding reverse intersystem crossing (rISC) rates of 0.6 and 1.6 × 10^5 s^{-1}, respectively. Unique in possessing both fast rISC and a relatively high PLQY, the unconventional **4-TPA-DBPzCN** regio-isomer turns out to be an efficient TADF emitter, highlighting the important role of donor–acceptor substitution position in the design of efficient TADF materials targeting specific wavelength ranges.

Received 26th March 2024,
Accepted 28th May 2024

DOI: 10.1039/d4tc01214c

rsc.li/materials-c

1. Introduction

The importance of organic light-emitting diodes (OLEDs) in the display industry has risen from novelty to dominance in the last decade. Global interest in this technology is further encouraged by the appealing advantages it can provide in terms of reduced energy consumption, compatibility with flexible substrates, large-scale processability, and tuneability of material properties.[1–3] Meanwhile, several challenges must still be overcome in the development of efficient OLED emitters, especially at the long wavelength edge of the visible spectrum. Indeed, emission in the deep red to near-infrared (NIR) region, commonly defined as the wavelength range between 650 and 1400 nm,[4] is required to enable multiple interesting applications such as night vision, fingerprinting, security/cryptography, light-based communication, and extending further to biomedical imaging, biosensors, and optical therapies.[5–11]

Unfortunately, the molecular design strategies for all-organic π-conjugated molecules that emit efficiently in this wavelength region are not straightforward. The absorption and emission bands of an organic emitter are typically red-shifted when the π-conjugated system is expanded, thereby lowering the optical gap.[12] While effective, this approach often triggers two unfavorable phenomena that result in quenching of the fluorescence: the 'energy gap' law and the formation of 'H-type' aggregates. The energy gap law states that the narrowing of energy gaps between the excited singlet states and the vibrational manifolds of the ground state – an inescapable consequence of the increased density of states as the singlet energy decreases – increases the rate of non-radiative decay losses through molecular vibrations.[13] This competes with the emissive decay mechanism, thereby reducing the fluorescence efficiency. While the rigidity of a π-conjugated system can help

[a] Hasselt University, Institute for Materials Research (IMO-IMOMEC), Design & Synthesis of Organic Semiconductors (DSOS), Agoralaan 1, 3590 Diepenbeek, Belgium. E-mail: wouter.maes@uhasselt.be
[b] IMOMEC Division, IMEC, Wetenschapspark 1, 3590 Diepenbeek, Belgium
[c] Energyville, Thorpark, 3600 Genk, Belgium
[d] University of Namur, Laboratory of Theoretical Chemistry, Theoretical and Structural Physical Chemistry Unit, Namur Institute of Structured Matter, Rue de Bruxelles 61, 5000 Namur, Belgium
[e] Durham University, Department of Physics, OEM group, South Road, Durham DH1 3LE, UK. E-mail: andrew.danos@durham.ac.uk
[f] Durham University, Department of Chemistry, South Road, Durham DH1 3LE, UK

† Electronic supplementary information (ESI) available. CCDC 2354499. For ESI and crystallographic data in CIF or other electronic format see DOI: https://doi.org/10.1039/d4tc01214c

to combat vibrational losses, the resulting molecular planarity can often simultaneously induce the formation of the aforementioned H-aggregates *via* undesired cofacial stacking. Emission from the lower excited (red-shifted) state of such 'excimer' aggregates is forbidden due to the out-of-phase orientation of the molecular transition dipoles, again resulting in a significant loss of fluorescence efficiency at practical doping concentrations of such emitters.[14]

While it is clear that smart material design can help to suppress the effects of both phenomena, additional focus must also be placed on maximizing device emission efficiency. In parallel with the photoluminescence quantum yield (PLQY), it is vital for emissive materials to be able to generate emission from both singlet and triplet excitons in the context of OLED operation. For 3rd generation OLEDs, upconversion of excitons from the non-emissive triplet state(s) to the first excited emissive singlet state *via* reverse intersystem crossing (rISC) allows this. Both rISC and consequent thermally activated delayed fluorescence (TADF) are supported by the available thermal energy of the environment, and become active when the energy difference between singlet and triplet states (or singlet–triplet energy gap, ΔE_{ST}) is minimized.[15,16] The design of charge-transfer (CT) TADF emitters that achieve such small ΔE_{ST} typically relies on the use of electron-donating and electron-accepting units, which maintain a twisted conformation along their connecting bond(s).[17] This gives rise to a minimal overlap between the highest occupied molecular orbital (HOMO) and lowest unoccupied molecular orbital (LUMO) localized on the donor and acceptor part, respectively, and hence a low exchange energy and small ΔE_{ST}.[18] However, some degree of overlap is still required as this supports the singlet emission oscillator strengths and higher quantum yields.[19] As such, careful and balanced molecular design and structural finetuning are both crucial for the development of novel high-performance TADF materials.

One strategy to potentially improve TADF properties entails the investigation of positional or regio-isomers *via* 'isomeric modulation'.[20–31] In the case of red TADF emitters, this generally involves the relocation of donor units and/or auxiliary acceptor groups (*e.g.* nitriles) on a rigid acceptor core and assessing how this affects the emission wavelength, PLQY, and TADF efficiency.[32–35] The dibenzo[*a*,*c*]phenazinedicarbonitrile (**DBPzCN**) acceptor scaffold is often employed in the design of red TADF emitters, and has multiple synthetically accessible sites for donor/acceptor attachment (Fig. 1).[36–45]

The extended π-conjugated system and significant rigidity of **DBPzCN** help to limit losses *via* non-radiative vibrational decay pathways.[46] Additionally, the incorporation of the N-heterocyclic moiety and nitrile groups enhance the electron-withdrawing capability of the acceptor significantly, further red-shifting the emission. By incorporating a pyrene moiety, Wang *et al.* and Shang *et al.* were recently able to access the previously unexplored 1(/8)-position of **DBPzCN** and thereby design novel TADF emitters.[21,24] To expand upon this work and assess the full set of regio-isomers, we attach a donor unit on the remaining unexplored 4(/5)-position of **DBPzCN** and fully characterize and compare the emissive properties of the resulting novel materials (Fig. 2).

In this study, four novel regio-isomers of (4-(diphenylamino)phenyl)dibenzo[*a*,*c*]phenazine-11,12-dicarbonitrile[47] (**TPA-DBPzCN**; Fig. 2) are computationally analyzed, synthesized, and photophysically characterized. Triphenylamine (TPA) is employed as a strong electron-rich donor unit for which the precursor is readily available. Time-dependent density functional theory (TDDFT) calculations are used to simulate the molecular geometries of the molecules and derive their associated singlet and triplet energy levels. Following the preparation of the different bromo-substituted phenanthrene-9,10-dione precursors, two synthesis strategies are tested and utilized to obtain the final materials. Compounds **2-TPA-DBPzCN**

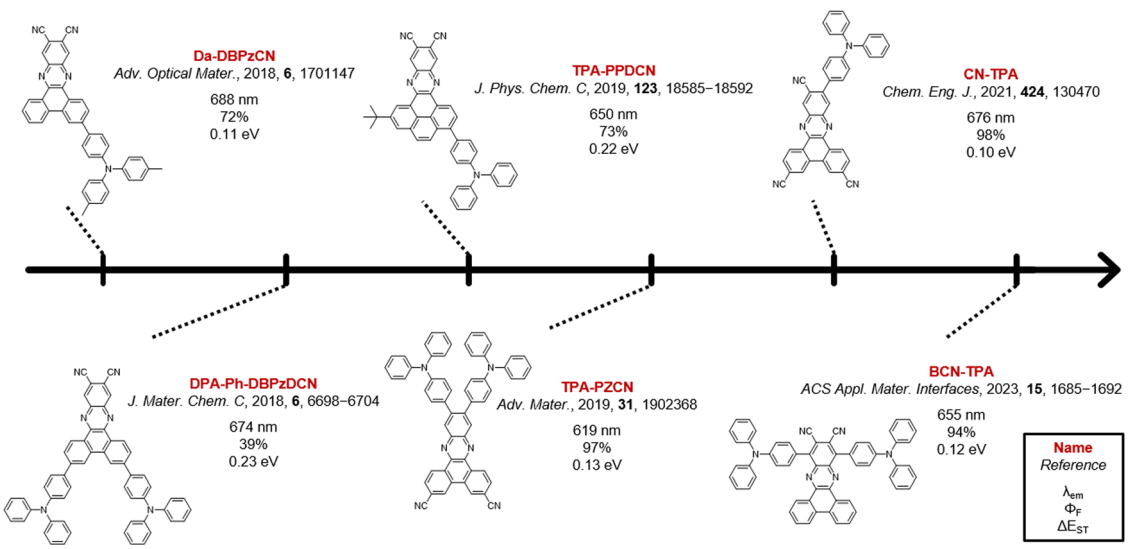

Fig. 1 Examples of reported red TADF emitters based on the **DBPzCN** acceptor. The main photophysical characteristics (emission wavelength, fluorescence quantum yield, and singlet–triplet energy gap) are given for the materials in doped films.

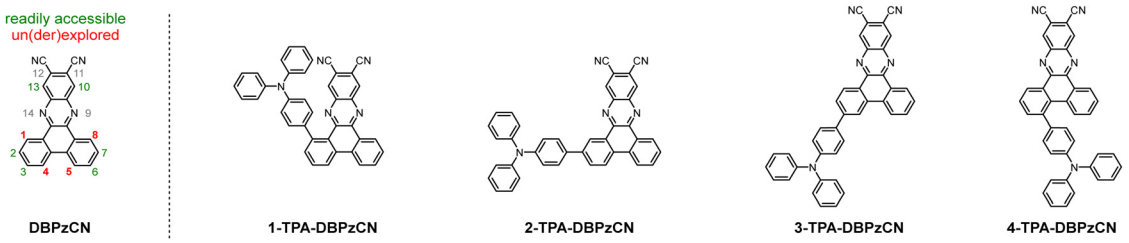

Fig. 2 Structural overview of the **DBPzCN** template (with numbered core positions) and the explored emitters **1-TPA-DBPzCN**, **2-TPA-DBPzCN**, **3-TPA-DBPzCN**, and **4-TPA-DBPzCN**.

and **3-TPA-DBPzCN** are readily synthesized from commercially available starting products, whereas **1-TPA-DBPzCN** and **4-TPA-DBPzCN** showcase the attachment of the donor unit on unconventional core positions. The four isomers are photophysically characterized in both solution and doped films, revealing significant differences between the isomers with regard to peak emission wavelength, PLQY, and TADF efficiency.

2. Results and discussion

2.1. Synthesis

2-Bromophenanthrene-9,10-dione and 3-bromophenanthrene-9,10-dione were purchased, while 1- and 4-bromophenanthrene were synthesized according to literature procedures and then oxidized to the respective phenanthrene-9,10-diones using chromium(VI) oxide (Scheme 1).[48,49] Two different strategies – referred to as pathway 'A' and 'B' – were then investigated to synthesize the final materials. In pathway A, the brominated phenanthrene-9,10-diones were first coupled to the triphenylamine donor unit using a Suzuki–Miyaura cross-coupling reaction. Subsequently, the acquired TPA-substituted phenanthrene-9,10-diones were used in an acid-catalysed condensation reaction with 4,5-diaminophthalonitrile. This produced isomers **2-**, **3-**, and **4-TPA-DBPzCN** in high yields, but was unsuccessful for the **1-TPA-DBPzCN** isomer, even under harsher conditions (see ESI†, Section S2). This is thought to be a result of the large steric hindrance in combination with the strong electron-donating capacity of the TPA donor unit. Accordingly, pathway B was designed, in which the order of the previous reactions was reversed. Although this method is complicated by the limited solubility of the Br-DBPzCN intermediates, isomers **2-** and **3-TPA-DBPzCN** were nonetheless obtained in high yields. **1-TPA-DBPzCN** was also successfully prepared, albeit in a lower yield of 20%, likely due to the still considerable steric hindrance and the poor solubility of the acceptor unit. The final materials underwent temperature-gradient vacuum sublimation to further purify them prior to their structural and photophysical characterization. Full details on the synthetic procedures and structural characterization data are provided in the Electronic ESI.†

2.2. Computational analysis and (TD)DFT calculations

DFT calculations using M06/6-311G(d) were performed to optimize the molecular geometries of isomer **1-**, **2-**, **3-**, and **4-TPA-DBPzCN**. Subsequently, singlet (S_1–S_2) and triplet (T_1–T_5) excited state energies were obtained using TDDFT calculations using a modified LC-BLYP (ω = 0.17 Bohr^{-1}) exchange–correlation (XC) functional.[50] These calculations were performed under the Tamm–Dancoff approximation[51] (TDA) and the polarizable continuum model (PCM) in cyclohexane to simulate a non-polar environment.[52] The Gaussian16 package was utilized to perform all calculations.[53] The orbital spatial distributions were obtained from single-point calculations using the same LC-BLYP(17)/6-311G(d) method. The CT character of the involved states was investigated by looking at the differences between ground and excited state electron densities. These CT characters are described by the distance over which the electronic charge is transferred (d_{CT}) and the related change in dipole moment ($\Delta\mu$), calculated as described by Le Bahers and

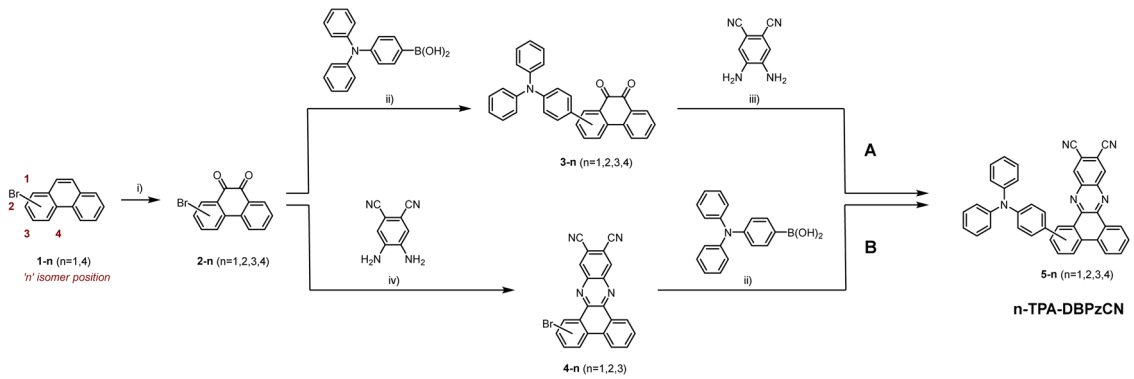

Scheme 1 Synthesis protocol for **1-TPA-DBPzCN**, **2-TPA-DBPzCN**, **3-TPA-DBPzCN**, and **4-TPA-DBPzCN**: (i) CrO_3, glacial acetic acid, reflux, 2 h; (ii) $Pd(PPh_3)_4$, Na_2CO_3, toluene, water, reflux, 24 h; (iii) HCl (37%), EtOH, THF, 40 °C, 24 h; (iv) glacial acetic acid, reflux, 24 h.

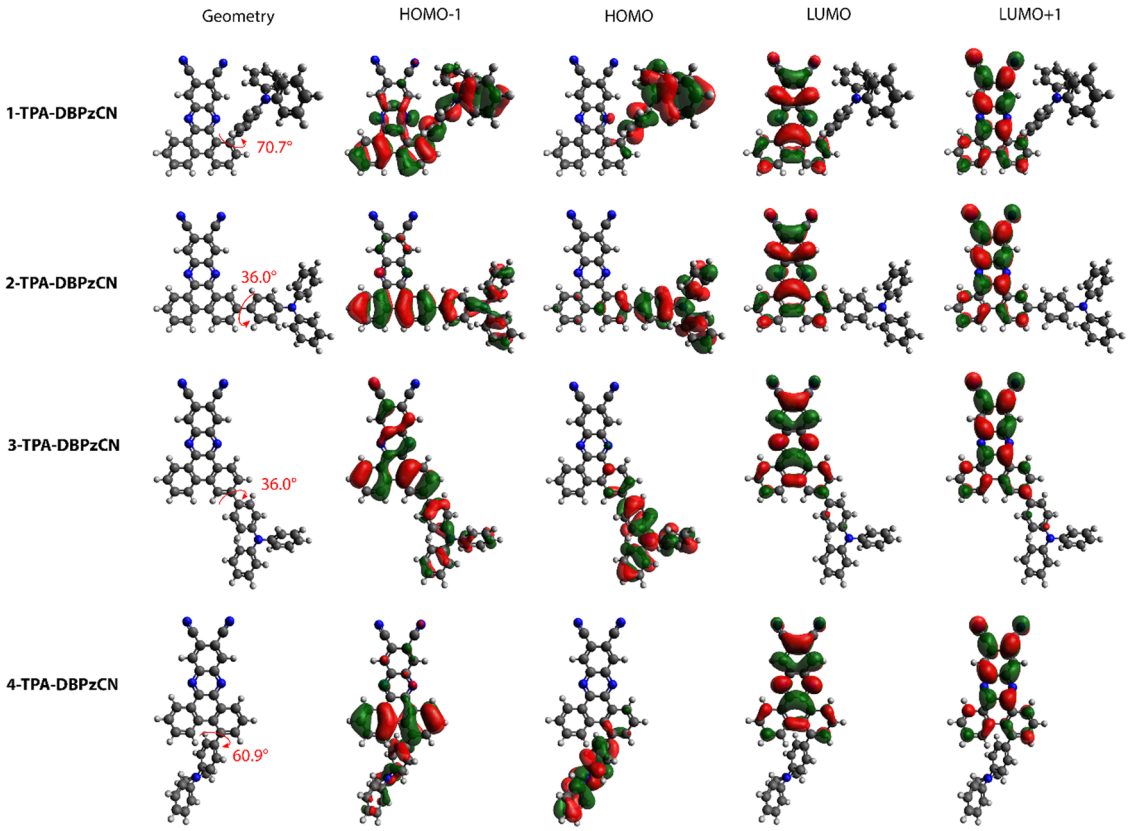

Fig. 3 Optimized molecular geometries and orbital spatial distributions (LUMO+1, LUMO, HOMO, and HOMO−1) for **1-TPA-DBPzCN**, **2-TPA-DBPzCN**, **3-TPA-DBPzCN**, and **4-TPA-DBPzCN**. Values of dihedral angles are given in red. Isocontour values of 0.02 (a.u.) were used for all orbitals.

coworkers.[54] Furthermore, the spin–orbit coupling (SOC) matrix elements were evaluated using the PySOC 23 program using the same XC functional, basis set, and PCM treatment as described above.[55]

Optimization of the molecular geometries reveals clear similarities as well as differences in the relative orientation (and dihedral angle) of the TPA and DBPzCN subunits between the different isomers (Fig. 3). Molecules **2**- and **3-TPA-DBPzCN** give a smaller dihedral angle ($\theta \approx 36^{\circ}$), not unexpected for a bond between TPA and a rigid but non-sterically constrained acceptor moiety.[56] Accordingly, both isomers **2**- and **3-TPA-DBPzCN** retain a relatively planar conformation where the donor unit lies roughly in the same plane as the acceptor unit (Fig. S3, ESI†). Significant differences are observed for the geometry of **1**- and **4-TPA-DBPzCN**. The increased steric hindrance pushes the TPA away from the acceptor core in **1-TPA-DBPzCN**, giving rise to a dihedral angle of around 71°. Meanwhile, **4-TPA-DBPzCN** exhibits a slightly smaller steric repulsion with the acceptor core, resulting in a dihedral angle of 61°. Furthermore, both **1**- and **4-TPA-DBPzCN** are expected to assume a distorted conformation as the donor unit is pushed outside of the plane of the acceptor (Fig. S3, ESI†).

Despite the clear differences in the calculated molecular geometries, the molecular orbital distributions are very similar for all four isomers. The HOMO is primarily localized on the TPA donor unit, whereas the LUMO and LUMO+1 can be found on the acceptor (Fig. 3). Superimposing the HOMO and LUMO distributions for each of the isomers shows a small overlap, thereby fulfilling the principal requirement of TADF molecular design. The main noteworthy difference in orbital distributions can be found for the HOMO−1. In **2**- and **4-TPA-DBPzCN**, this orbital is localized on the donor unit and the bottom part of the acceptor core, whereas **1**- and **3-TPA-DBPzCN** show a more delocalized orbital distribution onto the acceptor. As such, electron transitions that occur from the HOMO−1 might differ in their CT character.

From the TDDFT calculations, the nature, energy, and orbital distribution of the relevant excited states can be derived and compared. The first excited singlet states (S_1) of all isomers are characterized mainly by a HOMO to LUMO transition, from which their CT character becomes apparent (Table S1, ESI†). Proper investigation of the CT character of other (higher-lying) excited states requires a more in-depth analysis of the ground and excited state electron density differences (Table S1, S2 and Fig. S1, ESI†). These show the change of electron density in a molecule upon a transition from the ground state to a specific excited state. Changing electron densities in both the donor and acceptor unit (decreasing and increasing, respectively) are thus indicative of the CT nature of the excited state. When the changing electron densities are confined to the same unit (similar molecular distribution), the energy state is characterized as a locally excited (LE) state instead. Additionally, the strength of the spin–orbit coupling between a singlet and

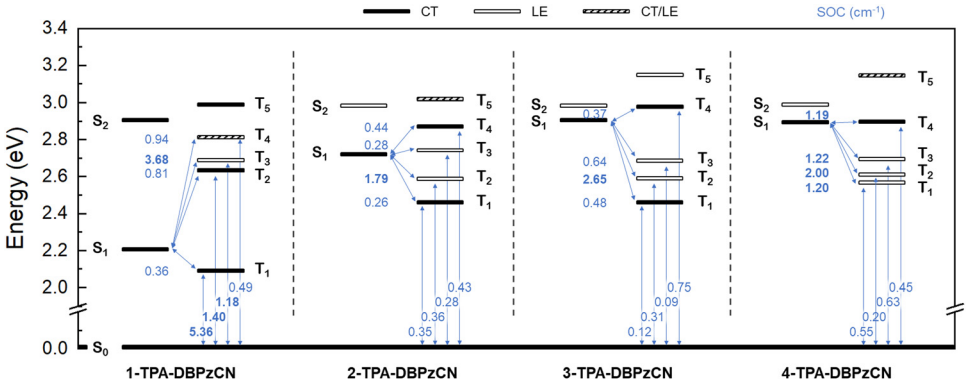

Fig. 4 Schematic overview of the excited state energy levels (in eV) of all four isomers with their corresponding CT (black), LE (white), and mixed CT/LE (dashed) character as obtained through TDDFT calculations. Relevant S_0–T_x and S_1–T_x (x = 1–5) couplings and SOC values are shown in blue (SOC values > 1 cm^{-1} in bold).

triplet state can be determined from the calculated SOC matrix elements. Together with the relative positions and orderings of the energy levels and the singlet–triplet gap, these values help to express the likelihood of a transition to occur between two specific states. A comprehensive excited state energy diagram is presented in Fig. 4, and also tabulated in the ESI† (Table S3, ESI†).

1-TPA-DBPzCN shows an interesting set of first excited (singlet and triplet) states which are relatively low in energy and noticeably separated from any higher states. With a small simulated ΔE_{ST} of 0.14 eV, good triplet upconversion could be envisaged. However, it is known that spin–orbit coupling between ^{1}CT and ^{3}CT states is forbidden under the requirement of total angular momentum conservation.[57] Instead, intersystem crossing occurs more readily between ^{1}CT and ^{3}LE states (according to the El Sayed rule[58]), and is promoted by vibronic coupling (VC) in case of rISC for D-A TADF materials.[59–61] As no neighbouring ^{3}LE states are present in proximity to T_1 (^{3}CT) to enhance upconversion *via* vibronic coupling, T_1 is expected to act as an exciton sink, despite the relatively small ΔE_{ST}.[59] This is further corroborated by the large SOC value for the transition from T_1 to the ground state (Fig. 4), allowing non-radiative deactivation and preventing efficient TADF.

A further comparison can be made between isomers **2-**, **3-**, and **4-TPA-DBPzCN**. The theoretical ΔE_{ST} decreases from 0.45 eV in **3-TPA-DBPzCN** to 0.32 eV in **4-TPA-DBPzCN**, and down to 0.27 eV in **2-TPA-DBPzCN** (Table S3, ESI†). In **2-TPA-DBPzCN**, upconversion from T_1 could be further enhanced by the presence of close-lying ^{3}LE states through vibronic coupling, with T_2 (LE) showing improved SOC and T_3 (LE) being nearly isoenergetic to S_1.[62] Intermediate ^{3}LE states between S_1 and T_1 are also present in **3-TPA-DBPzCN**, but these exhibit a much larger gap to S_1, which weakens the potential contribution of spin–vibronic coupling.[63] Similarly to **2-TPA-DBPzCN**, close-lying ^{3}LE states and an S_1-isoenergetic triplet state are also observed in **4-TPA-DBPzCN**. Furthermore, it is also noted that **4-TPA-DBPzCN** is the only isomer that has been simulated to have a T_1 state with LE character. This could allow SOC and upconversion to S_1 to compete with the decay from T_1 to the ground state, thereby diminishing non-radiative losses.[64] Furthermore, relatively large SOC values are observed for the transition between S_1 and T_1 (LE), T_2 (LE), T_3 (LE), and even T_4 (CT), despite its apparent CT character. In this case, upconversion could occur directly from T_1 (LE) – and potentially T_2 (LE) and T_3 (LE) – to S_1 (CT) through a combination of SOC and VC.[59,63] Alternatively, as the ΔE_{ST} of **4-TPA-DBPzCN** is relatively large, second-order non-adiabatic coupling might occur between T_1 (LE) and T_4 (CT).[65]

2.3. Photophysical characterization

Steady-state absorption and emission spectra were measured in toluene and zeonex host (Fig. 5). Several high-energy absorption bands can be observed below 450 nm for all 4 isomers in toluene, which are attributed to the π–π* and n–π* transitions occurring in the TPA and DBPzCN moieties.[47] The peak at around 360 nm is less defined for **1-** and **4-TPA-DBPzCN**, likely due to the distorted molecular geometry of the TPA unit. A relatively broad peak can be observed at longer wavelengths (>450 nm) which corresponds to the CT absorption band. The relative intensity of this CT band correlates with the calculated value of the oscillator strength for each isomer ($3 \gg 4 \approx 2 > 1$), which can be found in the ESI† (Table S3, ESI†). The emission spectra in toluene are comparable for each isomer, with exception of the shifted emission peak maximum for **2-** and **4-TPA-DBPzCN** compared to **1-** and **3-TPA-DBPzCN** (Fig. 5).

The fluorescence quantum yields (Φ_F) of all four isomers were determined in toluene solution to ascertain and compare their luminescence efficiency (Table 1). These measurements were performed under inert ($\Phi_{F,inert}$) and ambient air conditions ($\Phi_{F,air}$) to evaluate the impact of an oxygen-quenched triplet upconversion mechanism (Fig. S4, ESI†). The quantum yields in toluene solution are relatively low, with the notable exception of **3-TPA-DBPzCN**. The fluorescence improves from the "*cis*" molecular geometry in **1-TPA-DBPzCN** ($\Phi_{F,air}$ = 0.01) to the intermediate situation for **2-TPA-DBPzCN** ($\Phi_{F,air}$ = 0.05) to the "*trans*" molecular geometry in **3-TPA-DBPzCN** ($\Phi_{F,air}$ = 0.41). The unconventional geometry of **4-TPA-DBPzCN** results in an intermediate quantum yield ($\Phi_{F,air}$ = 0.11). Meanwhile, the quantum yields in oxygen-free toluene increase in tandem

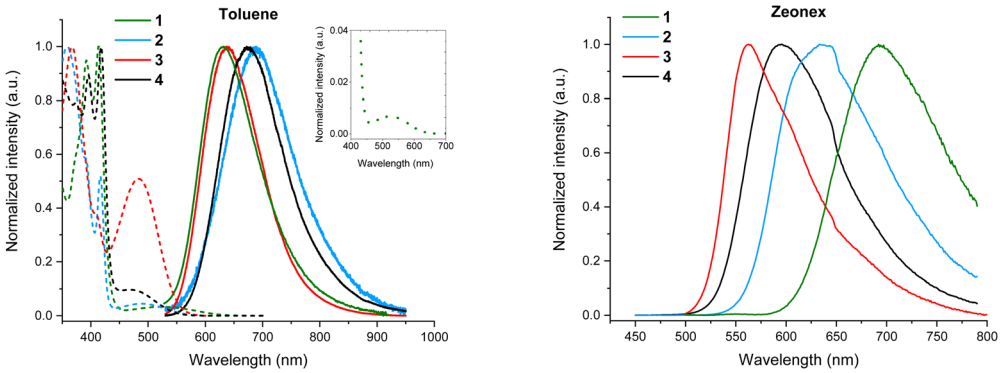

Fig. 5 Normalized steady-state absorption (dashed lines) and emission spectra (solid lines) for all four isomers in 10^{-5} M toluene solution (left, λ_{exc} = 440 nm) and emission spectra for 0.1 w/w% zeonex solid films (right, λ_{exc} = 440 nm). Graph inset (left) shows the magnified absorption spectrum of **1-TPA-DBPzCN**, revealing a weak CT absorption band. The inflexion around 650 nm in the emission spectra of all four isomers in zeonex film (right) is attributed to the onset of significant instrument-specific intensity correction at longer wavelengths.

Table 1 Spectroscopic parameters of the four emitters

Compound	$\lambda_{CT\ abs}$ [a] (nm)	λ_{em} [b] (nm) tol/zeonex	λ_{em} [c] (nm) CBP/DPEPO	$\Phi_{F,\ toluene}$ [d] air/inert	$\Phi_{F,\ zeonex}$ [e] air/inert	Φ_{Δ} [f]	HOMO/LUMO [g] (eV)
1-TPA-DBPzCN	536	632/692	707/727	0.01/0.02	<0.01/<0.01	0.27	−5.45/−3.61
2-TPA-DBPzCN	495	694/634	641/700	0.05/0.07	0.17/0.24	0.30	−5.51/−3.71
3-TPA-DBPzCN	484	630/564	660/700	0.41/0.52	0.47/0.46	0.58	−5.54/−3.64
4-TPA-DBPzCN	480	672/592	641/667	0.11/0.14	0.49/0.62	0.39	−5.57/−3.75

[a] CT band absorption maxima in toluene solution. [b] Fluorescence emission maxima in 10^{-5} M toluene solution and zeonex film (λ_{exc} = 440 nm). [c] Fluorescence emission maxima in CBP and DPEPO film (λ_{exc} = 440 nm). [d] Photoluminescence quantum yields in toluene solution under air and inert atmosphere relatively determined vs Coumarin 153 (Φ_F = 0.38, λ_{exc} = 440 nm in ethanol). [e] Absolute photoluminescence quantum yields in zeonex determined using an integrating sphere under air and inert atmosphere at room temperature (λ_{exc} = 440 nm). [f] Singlet oxygen quantum yields in toluene solution determined vs coronene (Φ_{Δ} = 0.90, λ_{exc} = 325 nm in toluene) by monitoring the absorbance of 1,3-diphenylisobenzofuran at 414 nm under emission from a secondary light source. [g] Determined from cyclic voltammetry (ESI, Section S7).

with the calculated oscillator strengths, improving the most for **3-TPA-DBPzCN** ($\Phi_{F,inert}$ = 0.52). Singlet oxygen quantum yields (Φ_{Δ}) were also determined in toluene solution, to investigate the formation of triplet states under standard air atmosphere (Fig. S5, ESI†). Molecular oxygen (which exists in the triplet ground state) can quench the populated excited triplet states of emissive materials, quantitatively forming singlet oxygen. As such, the higher singlet oxygen quantum yield of **3-TPA-DBPzCN** (Φ_{Δ} = 0.58) is indicative of the formation of longer-lived triplet states which can undergo some rISC in solution.

Additional steady-state absorption and emission spectra were measured in methylcyclohexane (MCH) and chloroform (CF) to investigate solvatochromic effects (Fig. S6, ESI†). The inherent broadness and observed red-shift of the emission bands in more polar solvents suggest a CT character for the emissive singlet state, as predicted by the TDDFT calculations. In chloroform, the strong stabilization of the CT state shifts the emission band beyond 700 nm, giving rise to NIR emission.

Next, the solid-state emission properties of doped films were investigated. Since the emitters show very low solubility ($\sim$0.1 mg mL^{-1} in toluene) and hence an assumed tendency to aggregate, low doping concentrations were utilized throughout. Separately, considerable acceptor π-stacking (interplanar distances of 3.61 Å) was observed in the single crystal X-ray structure of **3-TPA-DBPzCN** (the only material in this series that yielded usable crystals, Fig. S9, ESI†), lending credence to this assumed propensity towards aggregation. Firstly, 0.1 w/w% films in zeonex host were prepared. Zeonex has a non-conjugated polymer structure, allowing for the creation of smooth, homogenous films. Additionally, it exhibits a low polarizability (similar to MCH), which limits its influence on the stabilization of the CT states.[66] It is therefore often used to investigate the intrinsic solid-state TADF properties of novel compounds. When going from the more polar toluene solution to a zeonex film, a blue-shift in the emission maximum is typically observed (Fig. 5). This is true for zeonex films of **2-**, **3-**, and **4-TPA-DBPzCN**. Only **1-TPA-DBPzCN** shows a significantly red-shifted emission in zeonex, which can be attributed to its large tendency to aggregate (as correlated with its exceptionally poor solubility). The luminescence efficiencies are noticeably different in the zeonex host. Compared to in toluene solution, the quantum yields remain roughly the same for **1-TPA-DBPzCN** ($\Phi_{F,air}$ = <0.01) and **3-TPA-DBPzCN** ($\Phi_{F,air}$ = 0.47), while a decent increase is observed for **2-TPA-DBPzCN** ($\Phi_{F,air}$ = 0.17) and especially **4-TPA-DBPzCN** ($\Phi_{F,air}$ = 0.49). With the exception of **3-TPA-DBPzCN**, the quantum yield is even more enhanced in zeonex film when applying an inert atmosphere. This suggests an improvement of the triplet upconversion and the presence of a delayed fluorescence component, most pronounced for **2-TPA-DBPzCN** ($\Phi_{F,inert}$ = 0.24) and **4-TPA-DBPzCN** ($\Phi_{F,inert}$ = 0.62).

Two additional host materials were selected to investigate the effects of host nature and polarizability on the solid-state emission properties: 4,4′-bis(*N*-carbazolyl)-1,1′-biphenyl (CBP, E_T = 2.6 eV)[67] and bis[2-(diphenylphosphino)phenyl]ether oxide (DPEPO, E_T = 3.0 eV).[68] These small-molecule hosts are widely used in the development of OLEDs because of their excellent energy alignment and respective high hole or electron mobility. As the polar environment further stabilizes the CT emissive state relative to zeonex, a significant red-shift is observed in both 1 w/w% CBP and 1 w/w% DPEPO films, pushing the solid-state emission closer to the NIR (Fig. S10, ESI† and Table 1). Additional high-energy emission bands are revealed in both CBP and DPEPO films by changing the excitation wavelength from 400/450 to 350 nm. In CBP, these bands originate from (partial) excitation of the host, as confirmed by the measurement of a pure CBP film (Fig. S10, ESI†).[69] In DPEPO, it is possible that these signals arise from a distorted conformation which might become more prevalent in the strongly polar host. The higher relative intensity of these undesired emission bands in **1-TPA-DBPzCN** highlights its poor CT emission character, likely caused by the unfavourable twisted "*cis*"-geometry of the molecular structure.[24]

Time-resolved emission spectroscopy (TRES) experiments were then done to investigate the time-dependent emission mechanisms of the four emitters in zeonex films (as well as in CBP and DPEPO). Contour plots of the normalized time-resolved emission spectra of the zeonex films are shown in Fig. 6, while additional contour plots of the CBP and DPEPO films are provided in Fig. S11 and S12 (ESI†). For TADF emitters, three distinct emission phenomena can generally be identified at separate timescales, *i.e.* prompt fluorescence in the nanoseconds regime, delayed fluorescence in the micro- to milliseconds regime, and phosphorescence at the late milliseconds to seconds regime. Since classical phosphorescence is a forbidden transition, it is typically outperformed by non-radiative decay and thereby too weak to be observed at room temperature. Therefore, measurements are also done at 80 K to limit vibrational energy losses and analyse the phosphorescence emission to determine experimental T_1 energies.

At room temperature, initial fluorescence emission remains relatively constant for all four isomers up until a few hundred nanoseconds, when a small red-shift is observed for **3-** and (most clear for) **4-TPA-DBPzCN**. This shift is often attributed to the slower emission decay from shifted excited singlet states with slightly different molecular geometries, typically as a result of a changing dihedral angle between the donor and acceptor unit.[70,71] At 80 K, this shift can be more pronounced due to the (limited) rotational freedom of the phenyl moieties of the TPA donor unit. For **1-TPA-DBPzCN**, a rather unusual blue-shift appears to be observed at room temperature. However, investigation of the time-resolved emission spectra reveals the presence of a weak, second emission band which starts to dominate after the decay of the main prompt emission. Possibly linked to some rare molecular conformation of **1-TPA-DBPzCN**, this band might only become visible due to the low PLQY of the material's primary emission channel.

In the micro- to milliseconds regime, delayed emission is observed at the same wavelength as the prompt emission for **2-**, **3-**, and **4-TPA-DBPzCN**. This emission likely originates from the same singlet state (*i.e.* S_1), suggesting TADF. Isomers **2-** and especially **4-TPA-DBPzCN** show relatively strong delayed fluorescence which persists for the entire time window of the measurement, while the delayed emission of **3-TPA-DBPzCN** dips below the detection limit of the instrument for most of the early microseconds regime. Meanwhile, **1-TPA-DBPzCN** shows only delayed fluorescence intensity comparable with the baseline of the instrument, again likely resulting from the extremely poor PLQY of this particular material.

At 80 K, the delayed emission of **2-**, **3-**, and **4-TPA-DBPzCN** partially or completely disappears in the microseconds timeframe, as the triplet upconversion mechanism becomes thermally less accessible. Instead, a (small) red-shifted emission can be seen for **2-** and **3-TPA-DBPzCN** at a later timescale which represents the phosphorescence. Contrarily, a small blue-shift

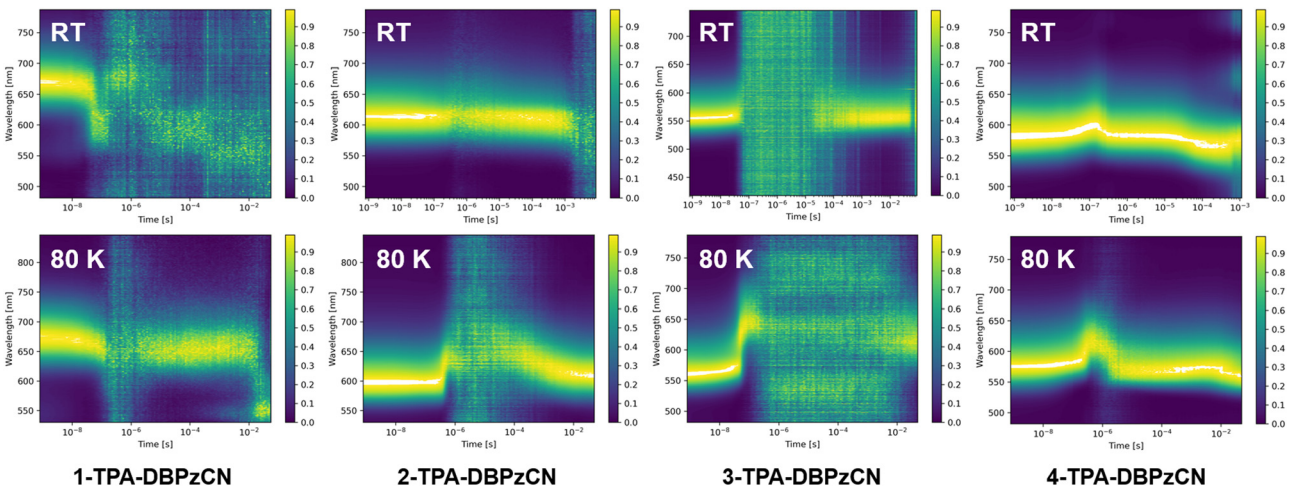

Fig. 6 Normalized time-resolved emission spectra (contour plots) for all isomers in 0.1 w/w% zeonex films (λ_{exc} = 355 nm) at room temperature (top row) and 80 K (bottom row).

Table 2 Experimental singlet–triplet gaps and derived kinetic properties of the four emitters in zeonex

Compound	ΔE_{ST} [a] (eV)	k_F [b] (10^7 s^{-1})	k_{ISC} [b] (10^6 s^{-1})	k_{rISC} [b] (10^5 s^{-1})
1-TPA-DBPzCN	/[c]	2.46	/[d]	/[d]
2-TPA-DBPzCN	0.027	0.91	9.33	0.19
3-TPA-DBPzCN	0.124	3.23	3.69	0.12
4-TPA-DBPzCN	~0	1.35	18.3	1.59

[a] Determined by taking the difference of the onset of the steady-state fluorescence band at room temperature and the 80-milliseconds delay-time phosphorescence band at 80 K. [b] Derived by applying a kinetic fitting model to the total emission decay curves.[72] [c] Could not be determined due to absence of measurable phosphorescence. [d] Could not be determined due to the absence of measurable delayed fluorescence.

is observed at a later timescale for **4-TPA-DBPzCN**, likely due to the LE nature of the T_1 state (as predicted by TDDFT). This is experimentally confirmed by the phosphorescence spectrum at 80 K, which shows some vibronic fine structure (Fig. S13, ESI†). Since residual delayed fluorescence and phosphorescence are visible at roughly the same wavelength as the prompt fluorescence in the contour plot of **4-TPA-DBPzCN** at 80 K, a minimal ΔE_{ST} is expected. This gap can be experimentally determined by subtracting the onset of the steady-state fluorescence spectrum at room temperature and the 80-millisecond delay-time phosphorescence spectrum at 80 K (Fig. S13, ESI† and Table 2). The smaller gap between the fluorescence and phosphorescence correlates with the increased intensity of the microsecond delayed fluorescence in the contour plots of **2-**, **3-** and **4-TPA-DBPzCN** in zeonex film at room temperature. As such, this supports our previous hypothesis of TADF being the proposed triplet upconversion mechanism.

Meanwhile, **2-**, **3-** and **4-TPA-DBPzCN** show rather comparable contour plot profiles in both CBP and DPEPO (Fig. S11 and S12, ESI†). Here, the CT emission band is rather poorly defined due to the limited luminescence intensity which drops below the noise baseline of the instrument at longer emission lifetimes. Unfortunately, the contour plots of **1-TPA-DBPzCN** in particular become quite unusable for characterising the CT emission bands in both CBP and DPEPO, as the high energy bands become more dominant.

Further comparison between the delayed emission properties can be made by plotting the total emission decay curves of the four isomers in zeonex. Fig. 7 shows the decrease of the total photon-count over time. The first descending curve represents the prompt fluorescence decay, whereas the second part shows the delayed fluorescence decay as a result of (delayed) triplet to singlet upconversion. The prompt fluorescence decay appears largely similar for all isomers, while the strongest and most rapid delayed emission component is observed for **4-TPA-DBPzCN**. The relative contribution of the delayed emission to the total photon-count remains largely consistent between **2-**, **3-**, and **4-TPA-DBPzCN** in CBP and DPEPO (Fig. S15, ESI†). However, the overall slope decreases when moving from zeonex to CBP and DPEPO films as a result of the larger polarizability and structural rigidity of the hosts.[66] For **1-TPA-DBPzCN**, only the prompt fluorescence decay could be plotted. This emission

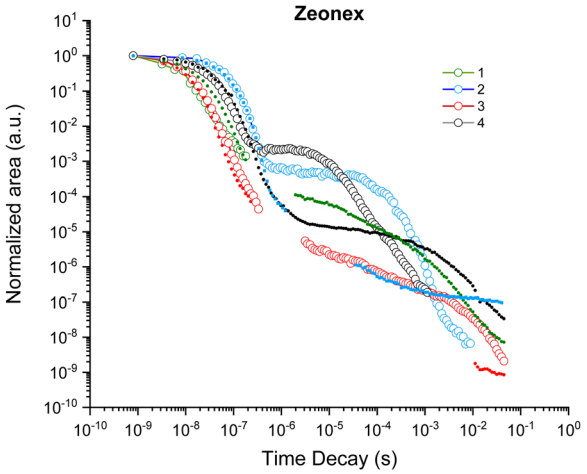

Fig. 7 Total emission decay (calculated *via* the integrated area under the emission curve) for **1-TPA-DBPzCN** (green), **2-TPA-DBPzCN** (blue), **3-TPA-DBPzCN** (red), and **4-TPA-DBPzCN** (black) at room temperature (open circles) and 80 K (closed circles). Data points with signal below the noise baseline have been omitted from the figure.

quickly disappears in zeonex and DPEPO, while a longer prompt emission is observed in CBP film.

Applying a kinetic fitting model to the double decay curve allows for the determination of important kinetic properties such as the fluorescence rate contant (k_F) and both the standard and reversed intersystem crossing rate constants (k_{ISC} and k_{rISC}, respectively).[72] The fitted values for these parameters are given in Table 2 (and Table S7, ESI† for CBP and DPEPO). Highest values for k_F are observed for **3-TPA-DBPzCN** and correspond to faster prompt fluorescence. Meanwhile, the k_{ISC} of **3-TPA-DBPzCN** appears to be smaller than those of **2-** and **4-TPA-DBPzCN**, indicating slower and less overall formation of populated triplet states following photo-excitation. This is particularly the case in zeonex films, where the largest differences between **3-TPA-DBPzCN** and the other isomers are apparent. Its derived higher k_F and lower k_{ISC} can be further corroborated by its high PLQY in film, which remains the same in both ambient air and inert atmosphere.

The most important difference in the kinetic properties of the isomer series can be found in the k_{rISC} values. k_{rISC} improves significantly going from **3-TPA-DBPzCN** ($\sim 1 \times 10^4$ s^{-1}) to **2-TPA-DBPzCN** ($\sim 2 \times 10^4$ s^{-1}) and finally to **4-TPA-DBPzCN** ($\sim 16 \times 10^4$ s^{-1}) in zeonex. Since the rate (and efficiency) of the rISC process are intrinsically linked to the size of the singlet–triplet energy gap (in addition to the nature of the relevant states), a relative increase in k_{rISC} should be expected when the ΔE_{ST} is minimized further. This trend is clearly illustrated in Table 2, where the minimal ΔE_{ST} of **4-TPA-DBPzCN** results in it possessing the best triplet upconversion in comparison to the larger ΔE_{ST} of **3-TPA-DBPzCN**. The substantially higher $k_{(r)ISC}$ values of **4-TPA-DBPzCN** in zeonex can be explained by the presence of its unique T_1 (LE) state. The LE nature of its triplet state enables faster (r)ISC through more efficient SOC with the CT S_1 state, in accordance to the El Sayed rule.[58] Interestingly, **2-TPA-DBPzCN** seems to express better TADF than **3-TPA-DBPzCN**,

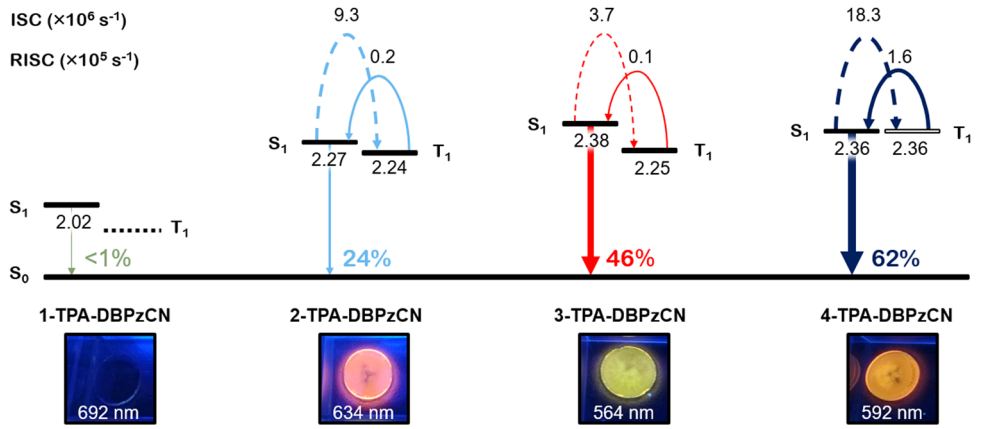

Fig. 8 Schematic overview of the main emission characteristics of **1-TPA-DBPzCN** (green), **2-TPA-DBPzCN** (blue), **3-TPA-DBPzCN** (red), and **4-TPA-DBPzCN** (black) in 0.1 w/w% zeonex films. The relative positions of the first excited singlet and triplet states are shown according to their experimentally determined energies (in eV), with the exception of the triplet state of **1-TPA-DBPzCN**. The corresponding CT (black) or LE (white) character of the excited state is also indicated. The photoluminescence quantum yields are expressed in percentages.

despite their seemingly identical molecular conformations, with the **3-TPA-DBPzCN** exhibiting a faster PF and an oxygen invariant film PLQY more reminiscent of purely fluorescent chromophores. Since **4-TPA-DBPzCN** also shows the largest increase in PLQY from air to inert atmosphere in zeonex, it clearly stands out as the best TADF emitter among the investigated regio-isomer series. Considering the rare utilisation of this substitution position in existing reports of TADF materials using this and similar acceptors, we envisage that the discovery of superior TADF in **4-TPA-DBPzCN** compared to its regio-isomers will stimulate further investigation of similarly substituted materials in future. A final comparison of the main emission characteristics for the four isomer materials in zeonex can be found in Fig. 8.

3. Conclusions

In this work, the influence of the regio-isomeric position of a triphenylamine donor on the standard and delayed emission properties of **TPA-DBPzCN** was investigated. Changes in relative orientation between the donor and acceptor subunits have a profound effect on the emission wavelength, photoluminescence quantum yield, and delayed fluorescence rate and efficiency. The twisted conformation and larger dihedral angles in **1-TPA-DBPzCN** and **4-TPA-DBPzCN** play an important role in changing their emission characteristics. Notwithstanding, different behaviour is even observed between **2-TPA-DBPzCN** and **3-TPA-DBPzCN**, which exhibit the same dihedral angle according to the TDDFT calculations. While **1-TPA-DBPzCN** shows the desired strongly red-shifted emission in different host materials, its emission is largely quenched. This is mainly attributed to the unfavourable molecular "*cis*" conformation and extreme twisting of the donor unit. Additionally, this conformation seems to give rise to a low-energy triplet trap state with large spin–orbit coupling to the ground state. **2-TPA-DBPzCN** shows surprisingly decent TADF characteristics despite its limited dihedral angle, possibly explained by a suitable alignment of both theoretical and experimental triplet and singlet energy states. Meanwhile, **3-TPA-DBPzCN** shows noticeably different emission behaviour. A relatively high fluorescence quantum yield is attributed to the favorable molecular "*trans*" conformation and larger oscillator strength. Unfortunately, the emission red-shift and TADF characteristics are rather poor in zeonex film, in which it acts more similarly to typical fluorescent dyes. Finally, **4-TPA-DBPzCN** is revealed as the overall best TADF emitter in this regio-isomer series. In zeonex, it exhibits the fastest (r)ISC rates and highest (increase in) quantum yield through improved S_1–T_1 spin–orbit coupling as a result of its near-zero ΔE_{ST} and unique ^{3}LE first excited triplet state. This series therefore showcases the importance of investigating underexplored structural motifs and substitution positions in progressing the design and properties of TADF emitters.

Conflicts of interest

There are no conflicts to declare.

Acknowledgements

The authors thank the Research Foundation – Flanders (FWO Vlaanderen) for financial support through projects G087718N, G0D1521N, I006320N, GOH3816NAUHL, the Scientific Research Community 'Supramolecular Chemistry and Materials' (W000620N), postdoctoral fellowship 1284623N (T. Cardeynaels), and PhD scholarship 1SC8621N (S. Brebels). The calculations were performed on the computers of the 'Consortium des équipements de Calcul Intensif (CÉCI)' (**https://www.ceci-hpc.be**), including those of the 'UNamur Technological Platform of High-Performance Computing (PTCI)' (**https://www.ptci.unamur.be**), for which we gratefully acknowledge financial support from the FNRS-FRFC, the Walloon Region, and the University of Namur (Conventions No. GEQ U.G006.15, U.G018.19, U.G011.22, RW/GEQ2016, RW1610468, and RW2110213). S. Kuila and A. P. Monkman are supported by EPSRC grant EP/T02240X/1.

We also thank Dr Dmitry S. Yufit of the Durham crystallography service for XRD measurements and technical support.

References

1 E.-L. Hsiang, Z. Yang, Q. Yang, Y.-F. Lan and S.-T. Wu, *J. Soc. Inf. Disp.*, 2021, **29**, 446–465.
2 G. Hong, X. Gan, C. Leonhardt, Z. Zhang, J. Seibert, J. M. Busch and S. Bräse, *Adv. Mater.*, 2021, **33**, 2005630.
3 H. Uoyama, K. Goushi, K. Shizu, H. Nomura and C. Adachi, *Nature*, 2012, **492**, 234–238.
4 M. Vasilopoulou, A. Fakharuddin, F. P. García de Arquer, D. G. Georgiadou, H. Kim, A. R. B. Mohd Yusoff, F. Gao, M. K. Nazeeruddin, H. J. Bolink and E. H. Sargent, *Nat. Photonics*, 2021, **15**, 656–669.
5 A. Minotto, P. A. Haigh, G. Łukasiewicz, E. Lunedei, D. T. Gryko, I. Darwazeh and F. Cacialli, *Light: Sci. Appl.*, 2020, **9**, 70.
6 Y. Khan, D. Han, A. Pierre, J. Ting, X. Wang, C. M. Lochner, G. Bovo, N. Yaacobi-Gross, C. Newsome, R. Wilson and A. C. Arias, *Proc. Natl. Acad. Sci. U. S. A.*, 2018, **115**, E11015–e11024.
7 C.-H. Lin, K. S. Karim and Y.-H. Tai, *SID Symposium Digest of Technical Papers*, 2020, 51, pp. 1855–1858.
8 C. Lian, M. Piksa, K. Yoshida, S. Persheyev, K. J. Pawlik, K. Matczyszyn and I. D. W. Samuel, *npj Flexible Electron.*, 2019, **3**, 18.
9 F. Zhang and B. Z. Tang, *Chem. Sci.*, 2021, **12**, 3377–3378.
10 S. Qi, S. Kim, V.-N. Nguyen, Y. Kim, G. Niu, G. Kim, S.-J. Kim, S. Park and J. Yoon, *ACS Appl. Mater. Interfaces*, 2020, **12**, 51293–51301.
11 F. Ni, N. Li, L. Zhan and C. Yang, *Adv. Opt. Mater.*, 2020, **8**, 1902187.
12 Y. Yamaguchi, Y. Matsubara, T. Ochi, T. Wakamiya and Z.-I. Yoshida, *J. Am. Chem. Soc.*, 2008, **130**, 16442.
13 R. Englman and J. Jortner, *Mol. Phys.*, 1970, **18**, 145–164.
14 N. J. Hestand and F. C. Spano, *Chem. Rev.*, 2018, **118**, 7069–7163.
15 C. Adachi, *Jpn. J. Appl. Phys.*, 2014, **53**, 060101.
16 T. J. Penfold, F. B. Dias and A. P. Monkman, *Chem. Commun.*, 2018, **54**, 3926–3935.
17 Y. Im, M. Kim, Y. J. Cho, J.-A. Seo, K. S. Yook and J. Y. Lee, *Chem. Mater.*, 2017, **29**, 1946–1963.
18 X.-K. Chen, *CCS Chem.*, 2020, **2**, 1256–1267.
19 Y. Tao, K. Yuan, T. Chen, P. Xu, H. Li, R. Chen, C. Zheng, L. Zhang and W. Huang, *Adv. Mater.*, 2014, **26**, 7931–7958.
20 M. K. Etherington, F. Franchello, J. Gibson, T. Northey, J. Santos, J. S. Ward, H. F. Higginbotham, P. Data, A. Kurowska, P. L. Dos Santos, D. R. Graves, A. S. Batsanov, F. B. Dias, M. R. Bryce, T. J. Penfold and A. P. Monkman, *Nat. Commun.*, 2017, **8**, 14987.
21 T. Yang, Z. Cheng, Z. Li, J. Liang, Y. Xu, C. Li and Y. Wang, *Adv. Funct. Mater.*, 2020, **30**, 2002681.
22 T. Yang, J. Liang, Y. Cui, Z. Li, X. Peng, S.-J. Su, Y. Wang and C. Li, *Adv. Opt. Mater.*, 2023, **11**, 2201191.
23 C. Zhou, Y. Liu, Z. Sun, H. Liu, L. Xu, D. Hu and J. Hu, *Dyes Pigm.*, 2022, **205**, 110488.
24 A. Shang, T. Lu, H. Liu, C. Du, F. Liu, D. Jiang, J. Min, H. Zhang and P. Lu, *J. Mater. Chem. C*, 2021, **9**, 7392–7399.
25 K. Zhang, J. Fan, C.-K. Wang and L. Lin, *Phys. Chem. Chem. Phys.*, 2021, **23**, 21883–21892.
26 S. Kothavale, W. J. Chung and J. Y. Lee, *J. Mater. Chem. C*, 2022, **10**, 6043–6049.
27 Z. Yang, X. Ge, W. Li, Z. Mao, X. Chen, C. Xu, F. Long Gu, Y. Zhang, J. Zhao and Z. Chi, *Chem. Eng. J.*, 2022, **442**, 136219.
28 W. Xie, M. Li, X. Peng, W. Qiu, Y. Gan, Z. Chen, Y. He, W. Li, K. Liu, L. Wang, Q. Gu and S.-J. Su, *Chem. Eng. J.*, 2021, **425**, 131510.
29 B. Liu, W.-C. Chen, R. Zhang, Q. Liu, H. Wei, W.-L. Wu, L. Xing, R. Wang, Y. Liu, S. Ji, H.-L. Zhang and Y. Huo, *Dyes Pigm.*, 2023, **216**, 111314.
30 N. A. Kukhta, H. F. Higginbotham, T. Matulaitis, A. Danos, A. N. Bismillah, N. Haase, M. K. Etherington, D. S. Yufit, P. R. McGonigal, J. V. Gražulevičius and A. P. Monkman, *J. Mater. Chem. C*, 2019, **7**, 9184–9194.
31 A. Danos, D. Gudeika, N. A. Kukhta, R. Lygaitis, M. Colella, H. F. Higginbotham, A. N. Bismillah, P. R. McGonigal, J. V. Grazulevicius and A. P. Monkman, *J. Mater. Chem. C*, 2022, **10**, 4737–4747.
32 Y. Xiao, H. Wang, Z. Xie, M. Shen, R. Huang, Y. Miao, G. Liu, T. Yu and W. Huang, *Chem. Sci.*, 2022, **13**, 8906–8923.
33 S. Kothavale, J. Lim and J. Yeob Lee, *Chem. Eng. J.*, 2022, **431**, 134216.
34 H. Ye, J. Yang, K. Stavrou, M. Li, F. Liu, F. Li, S.-J. Su and A. P. Monkman, *Dyes Pigm.*, 2023, **219**, 111568.
35 K. Rayappa Naveen, K. Prabhu CP, R. Braveenth and J. Hyuk Kwon, *Chem. – Eur. J.*, 2022, **28**, e202103532.
36 S. Wang, Y. Miao, X. Yan, K. Ye and Y. Wang, *J. Mater. Chem. C*, 2018, **6**, 6698–6704.
37 U. Balijapalli, R. Nagata, N. Yamada, H. Nakanotani, M. Tanaka, A. D'Aléo, V. Placide, M. Mamada, Y. Tsuchiya and C. Adachi, *Angew. Chem., Int. Ed.*, 2021, **60**, 8477–8482.
38 T. Yang, B. Liang, Z. Cheng, C. Li, G. Lu and Y. Wang, *J. Phys. Chem. C*, 2019, **123**, 18585–18592.
39 Y.-Y. Wang, Y.-L. Zhang, K. Tong, L. Ding, J. Fan and L.-S. Liao, *J. Mater. Chem. C*, 2019, **7**, 15301–15307.
40 T. Cardeynaels, S. Paredis, A. Danos, D. Vanderzande, A. P. Monkman, B. Champagne and W. Maes, *Dyes Pigm.*, 2021, **186**, 109022.
41 S. Kothavale, W. J. Chung and J. Y. Lee, *J. Mater. Chem. C*, 2020, **8**, 7059–7066.
42 F.-M. Xie, H.-Z. Li, G.-L. Dai, Y.-Q. Li, T. Cheng, M. Xie, J.-X. Tang and X. Zhao, *ACS Appl. Mater. Interfaces*, 2019, **11**, 26144–26151.
43 Y.-L. Zhang, Q. Ran, Q. Wang, Y. Liu, C. Hänisch, S. Reineke, J. Fan and L. S. Liao, *Adv. Mater.*, 2019, **31**, 1902368.
44 J.-L. He, F.-C. Kong, B. Sun, X.-J. Wang, Q.-S. Tian, J. Fan and L.-S. Liao, *Chem. Eng. J.*, 2021, **424**, 130470.
45 H. Wang, J. X. Chen, X. C. Fan, Y. C. Cheng, L. Zhou, X. Zhang, J. Yu, K. Wang and X. H. Zhang, *ACS Appl. Mater. Interfaces*, 2023, **15**, 1685–1692.

46 F.-M. Xie, X.-Y. Zeng, J.-X. Zhou, Z.-D. An, W. Wang, Y.-Q. Li, X.-H. Zhang and J.-X. Tang, *J. Mater. Chem. C*, 2020, **8**, 15728–15734.
47 R. Furue, K. Matsuo, Y. Ashikari, H. Ooka, N. Amanokura and T. Yasuda, *Adv. Opt. Mater.*, 2018, **6**, 1701147.
48 A. Urbano, A. M. del Hoyo, A. Martínez-Carrión and M. C. Carreño, *Org. Lett.*, 2019, **21**, 4623–4627.
49 T. Matsushima, S. Kobayashi and S. Watanabe, *J. Org. Chem.*, 2016, **81**, 7799–7806.
50 T. Cardeynaels, S. Paredis, J. Deckers, S. Brebels, D. Vanderzande, W. Maes and B. Champagne, *Phys. Chem. Chem. Phys.*, 2020, **22**, 16387–16399.
51 T. J. Penfold, *J. Phys. Chem. C*, 2015, **119**, 13535–13544.
52 S. Hirata and M. Head-Gordon, *Chem. Phys. Lett.*, 1999, **314**, 291–299.
53 M. J. Frisch, G. W. Trucks, H. B. Schlegel, G. E. Scuseria, M. A. Robb, J. R. Cheeseman, G. Scalmani, V. Barone, G. A. Petersson, H. Nakatsuji, X. Li, M. Caricato, A. V. Marenich, J. Bloino, B. G. Janesko, R. Gomperts, B. Mennucci, H. P. Hratchian, J. V. Ortiz, A. F. Izmaylov, J. L. Sonnenberg, D. Williams-Young, F. Ding, F. Lipparini, F. Egidi, J. Goings, B. Peng, A. Petrone, T. Henderson, D. Ranasinghe, V. G. Zakrzewski, J. Gao, N. Rega, G. Zheng, W. Liang, M. Hada, M. Ehara, K. Toyota, R. Fukuda, J. Hasegawa, M. Ishida, T. Nakajima, Y. Honda, O. Kitao, H. Nakai, T. Vreven, K. Throssell, J. A. Montgomery Jr., J. E. Peralta, F. Ogliaro, M. J. Bearpark, J. J. Heyd, E. N. Brothers, K. N. Kudin, V. N. Staroverov, T. A. Keith, R. Kobayashi, J. Normand, K. Raghavachari, A. P. Rendell, J. C. Burant, S. S. Iyengar, J. Tomasi, M. Cossi, J. M. Millam, M. Klene, C. Adamo, R. Cammi, J. W. Ochterski, R. L. Martin, K. Morokuma, O. Farkas, J. B. Foresman and D. J. Fox, *Gaussian16 Revision A03*, Gaussian, Inc., Wallingford CT, 2016.
54 T. Le Bahers, C. Adamo and I. Ciofini, *J. Chem. Theory Comput.*, 2011, **7**, 2498–2506.
55 X. Gao, S. Bai, D. Fazzi, T. Niehaus, M. Barbatti and W. Thiel, *J. Chem. Theory Comput.*, 2017, **13**, 515–524.
56 W. Shipan, Z. Cheng, X. Song, X. Yan, K. Ye, Y. Liu, G. Yang and Y. Wang, *ACS Appl. Mater. Interfaces*, 2017, **9**, 9892–9901.
57 H. S. Kim, S. H. Lee, S. Yoo and C. Adachi, *Nat. Commun.*, 2024, **15**, 2267.
58 M. A. El-Sayed, *J. Chem. Phys.*, 2004, **38**, 2834–2838.
59 M. K. Etherington, J. Gibson, H. F. Higginbotham, T. J. Penfold and A. P. Monkman, *Nat. Commun.*, 2016, **7**, 13680.
60 J. Gibson, A. P. Monkman and T. J. Penfold, *Chem. Phys. Chem.*, 2016, **17**, 2956–2961.
61 S. Paredis, T. Cardeynaels, S. Brebels, J. Deckers, S. Kuila, A. Lathouwers, M. Van Landeghem, K. Vandewal, A. Danos, A. P. Monkman, B. Champagne and W. Maes, *Phys. Chem. Chem. Phys.*, 2023, **25**, 29842–29849.
62 J. Gibson and T. J. Penfold, *Phys. Chem. Chem. Phys.*, 2017, **19**, 8428–8434.
63 P. K. Samanta, D. Kim, V. Coropceanu and J.-L. Brédas, *J. Am. Chem. Soc.*, 2017, **139**, 4042–4051.
64 N. Notsuka, H. Nakanotani, H. Noda, K. Goushi and C. Adachi, *J. Phys. Chem. Lett.*, 2020, **11**, 562–566.
65 Z. Yang, Z. Mao, C. Xu, X. Chen, J. Zhao, Z. Yang, Y. Zhang, W. Wu, S. Jiao, Y. Liu, M. P. Aldred and Z. Chi, *Chem. Sci.*, 2019, **10**, 8129–8134.
66 K. Stavrou, L. G. Franca and A. P. Monkman, *ACS Appl. Electron. Mater.*, 2020, **2**, 2868–2881.
67 M. A. Baldo and S. R. Forrest, *Phys. Rev. B: Condens. Matter Mater. Phys.*, 2000, **62**, 10958–10966.
68 Q. Zhang, T. Komino, S. Huang, S. Matsunami, K. Goushi and C. Adachi, *Adv. Funct. Mater.*, 2012, **22**, 2327–2336.
69 S. Bagnich, A. Rudnick, P. Schroegel, P. Strohriegl and A. Köhler, *Philos. Trans. R. Soc. London, Ser. A*, 2015, **373**.
70 F. B. Dias, J. Santos, D. R. Graves, P. Data, R. S. Nobuyasu, M. A. Fox, A. S. Batsanov, T. Palmeira, M. N. Berberan-Santos, M. R. Bryce and A. P. Monkman, *Adv. Sci.*, 2016, **3**, 1600080.
71 D. Kelly, L. G. Franca, K. Stavrou, A. Danos and A. P. Monkman, *J. Phys. Chem. Lett.*, 2022, **13**, 6981–6986.
72 N. Haase, A. Danos, C. Pflumm, A. Morherr, P. Stachelek, A. Mekic, W. Brütting and A. P. Monkman, *J. Phys. Chem. C*, 2018, **122**, 29173–29179.